Journal of Materials Chemistry C

PAPER

View Article Online
View Journal | View Issue

Cite this: J. Mater. Chem. C, 2019, 7, 10218

Quenching-assisted actuation mechanisms in core–shell structured $BiFeO_3$–$BaTiO_3$ piezoceramics†

Ilkan Calisir, [a] Annette K. Kleppe, [b] Antonio Feteira [c] and David A. Hall *[a]

Received 24th March 2019,
Accepted 29th July 2019

DOI: 10.1039/c9tc01583c

rsc.li/materials-c

Electromechanical actuation in piezoceramics is usually enhanced by creating chemically homogeneous materials with structurally heterogeneous morphotropic phase boundaries, leading to abrupt changes in ion displacement directions within the perovskite unit cell. In the present study, an alternative mechanism to enhance electromechanical coupling is found in both chemically and structurally heterogeneous $BiFeO_3$–$BaTiO_3$ lead-free piezoceramics. Such a mechanism is observed in a composition exhibiting core–shell type microstructure, associated with donor-type substitution of Ti^{4+} for Fe^{3+}, and is primarily activated by thermal quenching treatment. Here, we describe the use of *in situ* high-energy synchrotron X-ray powder diffraction upon the application of a high electric field to directly monitor the ferroelectric and elastic interactions between these composite-like components, formed as core and shell regions within grains. Translational short or long-range ordering is observed in the $BiFeO_3$-depleted shell regions which undergo significant structural alterations from pseudocubic $Pm\bar{3}m$ relaxor-ferroelectric in slow-cooled ceramics to rhombohedral $R3c$ or $R3m$ with long-range ferroelectric order in the quenched state. The strain contributions from each component are calculated, leading to the conclusion that the total macroscopic strain arises predominantly from the transformed shell after quenching. Such observations are also complemented by investigations of microstructure and electrical properties, including ferroelectric behaviour and temperature-dependent dielectric properties.

1. Introduction

Electromechanical coupling is a characteristic feature of piezoceramics attained through large ion displacements, which are generated in the unit cell, yielding observable mechanical strain in response to an applied electric field and *vice versa*. This coupling allows piezoceramics to be used as electroactive materials in a number of applications requiring mechanical actuation (actuators), acoustic and resonance (transducers and ultrasonics) and sensing (sensors).[1,2] To achieve high electromechanical sensitivity and piezoelectric coefficients in piezoceramics, there has been a tremendous effort to understand the origin of the high piezoelectric response in both lead-based and lead-free ceramics. Most investigations on the search for lead-free replacements (arising due to the worldwide legislation to reduce the use of hazardous substances such as lead-based oxides including all sectors),[3] aim to achieve at least an equivalent performance to that of lead-based compounds. The search has been mainly focused on identifying the region or boundary, known as the morphotropic phase boundary (MPB), where associated piezoelectric activities are optimised in a solid solution, including piezoelectric coefficient d_{33}, electrostrain x_{33}, relative permittivity ε_r and electromechanical coupling coefficient k_p, for example. Exhaustive compositional studies on the promising lead-free ceramics including sodium-bismuth-titanate (NBT)-, potassium sodium niobate (KNN)-, barium calcium zirconate titanate (BCZT)- and bismuth ferrite (BF)-based solid solutions have revealed the occurrence of such regions in those solid solutions, though the reported properties are often insufficient for use as a replacement for lead-based compounds.

Nevertheless, new findings and approaches are still being reported and intriguing properties demonstrated. Such investigations exploit the high flexibility of the perovskite structure, doping strategies, abundance of oxides and their combinations, and composition- or temperature-dependent phase transformations. Reported novel phenomena such as presence/role of incommensurate phases within multiphase coexistence region/boundary/points, ergodicity in relaxor ferroelectrics

[a] School of Materials, University of Manchester, M13 9PL, Manchester, UK. E-mail: david.a.hall@manchester.ac.uk
[b] Diamond Light Source Ltd, Harwell Science and Innovation Campus, OX11 0DE, Didcot, UK
[c] Department of Engineering and Maths, Sheffield Hallam University, S1 1WB, Sheffield, UK

† Electronic supplementary information (ESI) available. See DOI: 10.1039/c9tc01583c

and microstructure design approaches undoubtedly provide an alternative perspective on finding a green and multifunctional material.

$BiFeO_3$ (BF) is regarded as a special multiferroic compound and has attracted great attention as a room temperature multiferroic.[4] Its solid solutions with other ABO_3-type perovskite end-members have recently been of great interest amongst ferro-piezoelectric polar dielectric materials, particularly after the issues associated with inherent high leakage current[4] and phase decomposition[5] were addressed successfully *via* doping[6–8] and synthesis strategies.[9] Particular attention can be drawn to $BiFeO_3$–$BaTiO_3$ (BF–BT) solid solutions, which have been intensively studied as promising candidates for high temperature piezoceramic applications,[8,10,11] surpassing the temperature capability of typical lead-based ferroelectrics. To date, the highest d_{33} in xBF–BT ceramics was reported as 402 pC N^{-1}, with a small amount of $BiGaO_3$ being incorporated in the composition with x = 0.67; these ceramics were prepared by water-quenching and were assumed to have an MPB composition, with coexistence of rhombohedral and tetragonal phases.[10] However, this report still remains as the only one showing such a high d_{33} and claiming the presence of a rhombohedral and tetragonal phase boundary in a BF–BT-based solid solution.

Intriguingly, the influence of quenching treatment regardless of the factors such as cooling methods[10,12] (*e.g.* liquid nitrogen, water, air, NaCl solution) and type of dopants,[10,13,14] is readily accepted as an effective means to modify the piezo-ferroelectric performance in BF-based ceramics, including pristine $BiFeO_3$.[9] However, the underlying mechanism is yet to be understood fully and is under debate.[7,13,15,16] On the other hand, in conventional type ferroelectrics such as acceptor-doped hard PZT and BT-based ferroelectrics, the quenching-induced enhancement in polarisation switching behaviour is mainly attributed to the randomization of dipolar defect associates, which generally become oriented along the local domain polarisation direction during an extended ageing period at room temperature and thereby act to constrain domain wall motion.[17]

The present work aims to shed light on the origin of enhancement in the electromechanical coupling as a result of thermal quenching treatments in BF–BT solid solutions. A fine compositional adjustment involving the incorporation of 1 mol% Ti^{4+} as a donor substitution for Fe^{3+} has been applied to the selected composition. Donor dopants play a key role in soft PZT ceramics, improving insulation resistance, enhancing domain wall mobility and hence increasing the piezoelectric performance.[18] In contrast, for BF–BT ceramics we have recently demonstrated that donor-doping with La^{3+} substituted for Ba^{2+} resulted in a unique core–shell type microstructure as a result of chemical phase segregation on the micro- and nano-scale, leading to significant degradation in polarisation switching.[6] Moreover, the application of quenching significantly altered the crystal structure in the shell regions, accompanied by a dramatic enhancement in polarisation.

In the present study, the effect of quenching on the actuation mechanisms in core–shell structured BF–BT composition and its influence on the phase assemblages have been revealed by using *in situ* high-energy synchrotron diffraction techniques. The results of these investigations provide an unprecedented insight into the understanding of this novel actuation mechanism, thereby providing a route to tailor the electromechanical responses of newly-designed piezoceramics in future.

2. Results and discussion

Ti-substituted BF–BT ceramics were synthesised by the solid state reaction method, based on the chemical formula of $0.75Bi(Fe_{1-x}Ti_x)O_3$–$0.25BaTiO_3$ with x = 0.01, 0.03 and 0.05. Sintered ceramics were annealed at 800 °C for 20 min and then divided into two groups based on the cooling procedure employed, which was either (a) a slow cooling rate of 300 °C h^{-1} or (b) air-quenching to room temperature. The ceramic samples resulting from these procedures are hereafter denoted as either slow-cooled and quenched. Further details of the processing and characterisation methods are provided in the ESI.†

2.1 Phase content and microstructure

Micrographs and X-ray diffraction patterns of 1 mol% Ti substituted-$0.75BiFeO_3$–$0.25BaTiO_3$ (BF–BT–1Ti) ceramics, for both slow-cooled and quenched states are presented in Fig. 1. Microstructural examination of the chemically-etched polished surfaces of the sintered ceramics is also shown in Fig. 1(a) and (b), respectively. The appearance of ferroelectric-type domain structures can be clearly observed for both slow-cooled and quenched states. However, the domain features are mainly concentrated in the central regions of the grains after slow cooling, while quenching led to additional domain features between the grain boundaries and the centres of the grains. Such features led us to investigate the polished surfaces without the application of etching; the occurrence of chemical heterogeneity was qualitatively confirmed using SEM in back-scattered electron (BSE) mode at high energy, as shown Fig. 1(c). It is apparent that the grain boundaries and most grain centres consist of heavier elements giving lighter contrast under BSE mode, indicating that those regions are bismuth-rich, while the darker regions are lacking in bismuth, which is the heaviest element relative to Fe, Ba and Ti.

Since the solid solution is primarily composed of two perovskite phases, with end members $BiFeO_3$ and $BaTiO_3$, the observed regional contrast could be due to phase separation of these two components as a result of both thermodynamic and kinetic factors. This issue has been discussed in detail in our previous investigations of $BiFeO_3$–$BaTiO_3$ ceramics.[7] It is also noted that minor amounts of impurities were detected, which appeared as the brightest contrast and could indicate the presence of expelled or excess bismuth oxide. The segregated phases, determined as $BiFeO_3$-rich and -depleted regions, will hereinafter be referred to as core and shell regions, respectively. These results provide microstructural evidence of chemical heterogeneity at the micro-scale and will be used as the basis of discussions in the following sections. Note that although 1 mol% Ti-doped ceramics are the main focus of the present

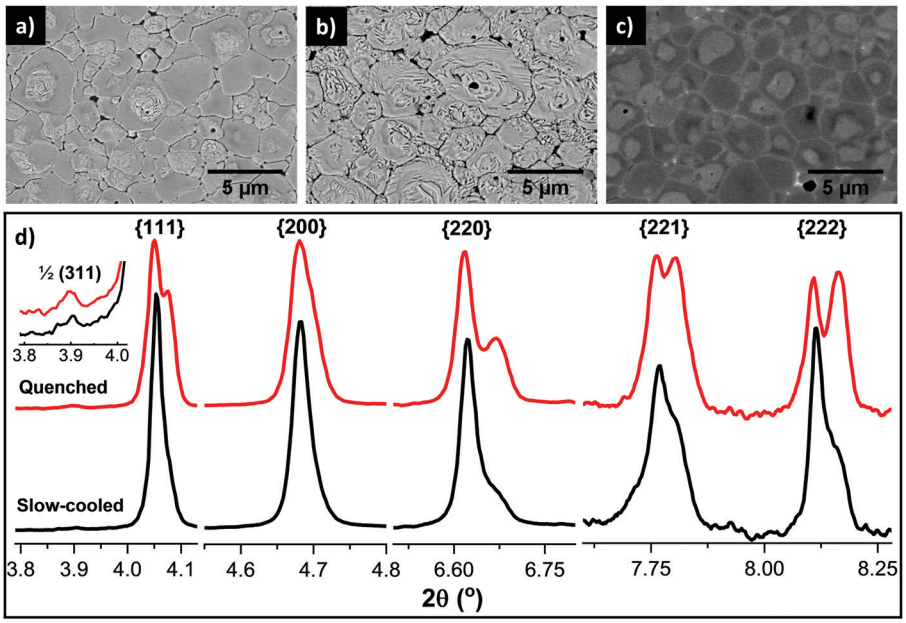

Fig. 1 SEM micrographs and high-energy (76 keV) XRD patterns of the BF–BT–1Ti ceramics. Chemically-etched surfaces of (a) slow-cooled and (b) quenched ceramics, and (c) non-etched polished surface of the quenched ceramic. (d) High-energy XRD profiles of slow-cooled and quenched ceramics for given crystallographic orientations; inset figure shows the super-lattice reflections of 1/2(311) for slow-cooled and quenched ceramics.

study, further systematic studies were also carried out, including doping levels up to 5 mol% Ti. The micrographs given in the ESI† (Fig. S1), show that highly uniform and homogeneous grain-domain types were obtained for the undoped composition, while further doping of Ti (>1 mol%) in BF–BT–Ti composition results in increased amounts of Bi-rich secondary phases, together with a reduced volume fraction of core regions.

The aforementioned chemical and domain heterogeneity within grains was also qualitatively confirmed using high-energy X-ray diffraction, as illustrated by the detailed peak profiles of particular crystallographic orientations for {111}, {200}, {220} and {222} shown in Fig. 1(d). The slow-cooled samples show a pseudocubic structure, which is discernible by the absence of preferred orientation, namely lack of splitting of the {111} and {200} peaks. However weak additional peaks were evident along with the main pseudocubic reflections at higher scattering angles, corresponding to {220}, {221} and {222} reflections, thereby suggesting a coexistence of multiple phases. Furthermore, the application of quenching caused pronounced peak splitting of {111} and significant broadening of {200} peaks. This observation strongly suggests that the crystal structure, which is multiphase due to the formation of the core–shell microstructure, undergoes significant transformations upon quenching.

Of particular note is a weak peak at $2\theta \approx 3.9^\circ$ in Fig. 1(d), representing the super-lattice peak, which is indexed as 1/2(311) with respect to the pseudocubic unit cell. It is visible in the diffraction patterns obtained from both ceramics. This superlattice reflection corresponds to the $a^-a^-a^-$ tilt system in the space group *R3c* in Glazer's notation.[19] It is due to oxygen planes caused by antiferrodistortive rotation of oxygen octahedra with an antiphase tilt in relation to the neighbouring octahedra,[5] and thus it has a low intensity due to the weak interactions between X-rays and light ions such as oxygen. Since the microstructural evidence suggests that the core is present in both cases without any prominent changes, in comparison with those in the transformed shell, it is concluded that the observed superlattice peak in both patterns corresponds to the common phase of the $BiFeO_3$-rich core.

2.2 Structural analysis

In the light of these observations, full-pattern refinement was performed to identify the crystal structures of the phases present. The high-energy X-ray diffraction patterns for the *in situ* study were recorded on the panel detector, yielding 2D Debye–Scherrer diffraction rings that provide an insight into the full range of grain orientations as a function of crystallographic orientation (Fig. 4(a)). However, among these rings there is one specific orientation angle, satisfying the relation $\cos^2\psi = 1/3$, $\psi = a\cos\left(1/\sqrt{3}\right) = 54.7^\circ$, which can be used for full-pattern structural refinement even after poling under a high electric field.[20] At this orientation, the domains are randomly oriented and therefore crystallographic texture is almost negligible. Furthermore, the elastic lattice strains associated with the development of inter-granular stresses are close to zero at this orientation, which facilitates the refinement of crystal structure and calculation of phase fractions without the need to incorporate models for the domain and strain orientation distribution functions (DOD and SOD, respectively).

After the determination of the specific orientation angle required for the full pattern refinement, the structural model was first constructed based on rhombohedral symmetry with *R3c* space group, which is the well-known crystal structure

of $BiFeO_3$.[4,5,9] However, it was found that the single phase model could not resolve the structure properly and therefore another crystal symmetry, pseudocubic $Pm\bar{3}m$, which is commonly assigned for xBF–BT ceramics ($x < 75\%$),[21–24] was added into the model. The refinement was significantly improved. However, the $R3c + Pm\bar{3}m$ model is only reasonable for the slow-cooled state since the $R3c$ phase corresponds to the ferroelectric core, while the featureless shell could comprise the non-polar $Pm\bar{3}m$ phase. On the other hand, it is not appropriate for the quenched state since the appearance of ferroelectric domains in the shell appears to indicate the transformation from non-polar or relaxor $Pm\bar{3}m$ to a polar ferroelectric $R3c$ configuration. To simplify the model for both states, a new binary model was designated as comprising $R3c^{Core}$ and $R3c^{Shell}$ phases, which serves to represent the core and shell regions in both the slow-cooled and quenched states, as illustrated in Fig. 2(a) and (b). According to this simplified approach, the pseudocubic phase can be represented by a rhombohedral structure with near-zero rhombohedral distortion.

The structural parameters obtained from the refinement are summarised in Table S1 (see the ESI†). It is evident that the $R3c$ phase fractions of the core and shell regions changed significantly as a result of the quenching process, although deviations in the unit cell parameters were minimal. Although $R3c$ crystal symmetry is used in the hexagonal setting for the refinement, it is more convenient to convert the hexagonal lattice parameters (a_h and c_h) into the pseudocubic setting, calculated as below:

$$a_{pc} = \sqrt[3]{\frac{\sqrt{3}a_h^2 c_h}{12}} \quad (1)$$

For the refinement procedure, the bismuth ions were situated on the A-site together with barium, and the substituent titanium ions were situated on the B-site together with iron. In order to obtain consistent refinement results, similar sets of parameters were used for all refinements. Although the grains are compositionally graded as $BiFeO_3$-rich and $BaTiO_3$-rich regions, the occupancies of A- and B-site ions were fixed based on the stoichiometry of $0.75Bi(Fe_{0.99}Ti_{0.01})O_3$–$0.25BaTiO_3$, since it may bring more complexity, and hence instability, into the refinement procedure if the occupancies were to be refined. As the isotropic thermal parameters, U_{iso}, were refined, a problem emerged in that there was a drastic increase in the U_{iso} value of the A-site compared with that of the B-site for both $R3c^{Core}$ and $R3c^{Shell}$ symmetries. This clearly indicates that the distributions of A- and B-site ions are not homogeneous within the assigned crystal structure. In fact, this is confirmed by the microstructural investigation discussed above. By combining results of structural refinement and microstructural observations it can be recognised that large deviations in the isotropic thermal parameters could be a useful indicator of chemical heterogeneity.

Another important parameter in structural analysis is the lattice distortion and associated inter-axial angles. The rhombohedral lattice distortion, η_{rh} can be calculated by eqn (2)[25] while the relation between the lattice inter-axial angles for rhombohedral, α_{rh}, and pseudocubic, α_{pc}, is given in eqn (3).[26]

$$\eta_{rh} = \left[\frac{\sqrt{2}c_h}{3\sqrt{2}a_h}\right] - 1 \quad (2)$$

$$90 - \alpha_{pc} = \left(\sqrt{3}/2\right)(60 - \alpha_{rh}) \quad (3)$$

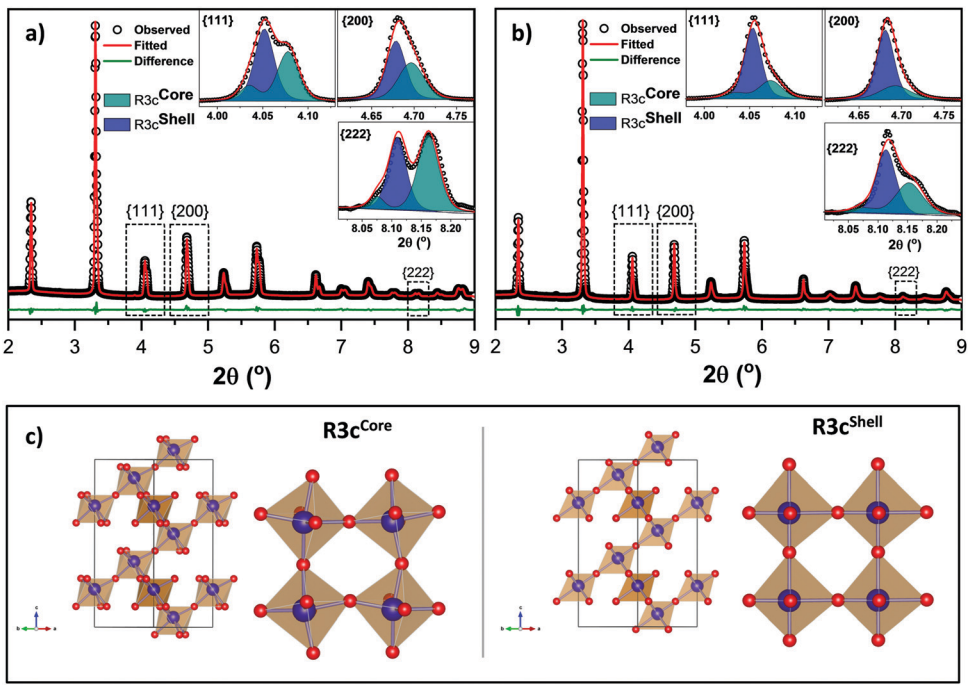

Fig. 2 Full-pattern structure refinement of (a) quenched and (b) slow-cooled BF–BT–1Ti ceramics. (c) $(Fe/Ti)O_6$ octahedral illustrations of core and shell structures in the quenched state.

The values of α_{rh}, were found to be 59.53° and 59.47° for the core regions of the slow-cooled and quenched ceramics, respectively, while the corresponding angles for the shell regions ($R3c^{Shell}$) are 59.96° and 59.92°, which exhibited minimal deviation with respect to primitive rhombohedral symmetry ($\alpha_{rh} \cong 60°$), yielding α_{pc} = 89.97° and 89.93° in the pseudocubic setting, as listed in Table S1 of the ESI.† The inter-axial angle in pristine $BiFeO_3$[27] is reported as α_{rh} = 59.35°. This value is comparable to the observed distortion in the $R3c^{Core}$ for both states, suggesting that the assigned crystal structure for the core is close to that of $BiFeO_3$.

To demonstrate the differences between the core and shell structures sharing *R3c* symmetry in the quenched state, a crystallographic information file (CIF) was generated from the refinement and illustrated in Fig. 2(c). It is evident that the distortions of the $(Fe/Ti)O_6$ octahedra are clearly distinguished between the core and shell structures. The Fe–O–Fe angle for $BiFeO_3$ itself is reported as 154.1°.[27] Therefore, it can be deduced that the regions with high $BiFeO_3$ phase content are responsible for the observed large distortions in the octahedra, yielding a B–O–B angle of 157.4°, for the quenched state, commensurate with the occurrence of $a^-a^-a^-$ tilt. On the other hand, suppression of octahedral tilting and a slight deviation in the B–O–B angle of the shell could be an indication of untilted *R3c*, namely *R3m*, as similarly observed in $0.75Bi(Fe_{2/8}Mg_{3/8}Ti_{3/8})O_3$–$0.25BaTiO_3$ reported by Dolgos *et al.*[28] The origin of such contrasting character could be due to large differences in ionic radii of the A-site ions (r_{Ba} = 1.61 Å and r_{Bi} = 1.45 Å) since the shell phase is $BiFeO_3$-depleted. This confirms the correlation between tilting and cation size of A-site ions as reported by Megaw,[26] suggesting that reduction in the radii of the A-cations in relation to octahedron edge length, l ($(r_A + r_{Oxygen})/l$) causes the suppression of octahedral tilting.

2.3 Dielectric and ferroelectric properties

The results presented in Fig. 3 illustrate the ε_r–T and P–E relationships for the slow-cooled and quenched BF–BT ceramics. In the former case, a lower-temperature dielectric anomaly is evident in the vicinity of $T_m^1 \approx 400$ °C; whilst with further heating another dielectric maximum is apparent at a higher temperature $T_m^2 \approx 625$ °C for both slow-cooled and quenched states. However, a dramatic increase in the magnitude of ε_r near T_m^1 was observed in the quenched ceramic, but the magnitude was relatively suppressed and diffuse with a marked frequency-dependence for the slow-cooled ceramic. Such changes in the magnitude of ε_r can be understood on the basis of the increase in intrinsic polarizability near the phase transition temperatures, while the frequency dispersion is a typical signature of relaxor ferroelectric behaviour. In common with our previous publications,[6,7] we attributed the transitions at T_m^1 and T_m^2 to contribution from the shell and core regions, respectively.

Variations in dielectric loss, tan δ, as a function of temperature and frequency for slow-cooled and quenched ceramics are shown in Fig. S3 (ESI†). Multiple anomalies in the dielectric permittivity are clearly observed in the cases of slow-cooled and quenched ceramics (Fig. 3a and b), whereas there is only one loss peak in the region of the Curie point, at a temperature of 575 °C, becoming more pronounced for the quenched case. This may be due to increased ferroelectric domain wall density after the quenching operation, which accordingly leads to higher dielectric loss near the Curie temperature. It is also observed that dielectric loss increases rapidly above 400 °C due to high electrical conductivity, as commonly reported in $BiFeO_3$-based ceramics.[7–11] Dielectric loss responses in the core and shell regions are masked by the observed high conductivity and thus cannot be easily distinguished.

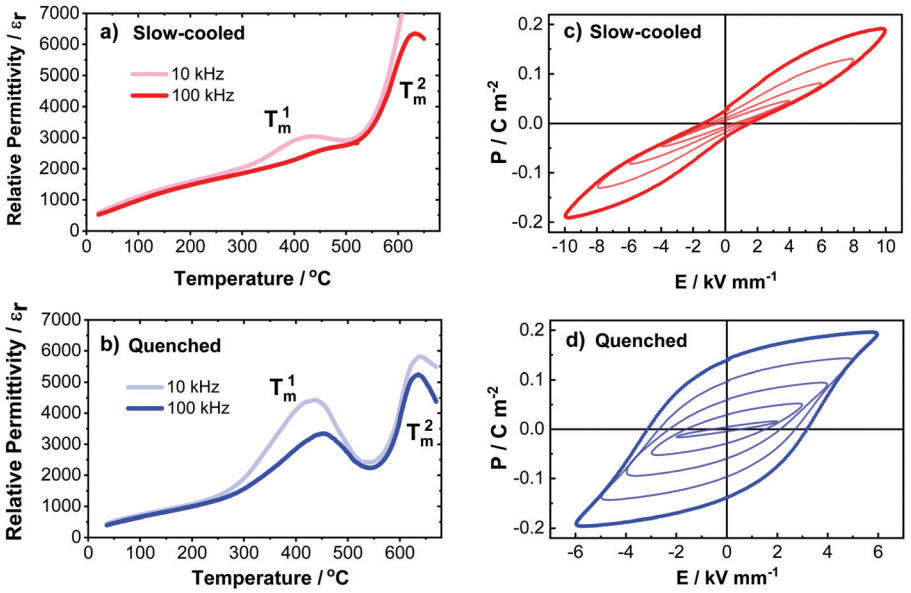

Fig. 3 Temperature-dependence of the relative permittivity measured at 10 kHz and 100 kHz in (a) slow-cooled and (b) quenched BF–BT–1Ti ceramics. P–E relationships in (c) slow-cooled and (d) quenched ceramics. Inner loops are measured upon increasing the electric field to show the progression of the polarisation switching mechanism.

Ferroelectric *P–E* hysteresis loops for the slow-cooled and quenched ceramics are shown in parts (c) and (d) of Fig. 3, respectively. For the slow-cooled state, constricted *P–E* loops were obtained under AC electric fields with magnitude up to 10 kV mm^{-1}. This constrained switching behaviour is attributed to the presence of polar nanodomains, commonly found in relaxor ferroelectric phases, indicating that oriented ferroelectric domains developed under high electric fields are unstable and cannot be retained after the removal of the field. It is evident that at a moderate electric field (E = 5 kV mm^{-1}), an almost linear response was recorded. According to the common interpretation given in the literature for such cases, it is linked to the transformation of randomly oriented polar nano regions (PNRs) to ordered ferroelectric domains, leading to the observed increase in polarization, while upon removal of the electric field the developed domains are dispersed into discrete PNRs, thus leading to almost zero net polarization at zero field.[29] Nevertheless, upon further increasing the field to 10 kV mm^{-1}, the loop transformed into a more open shape around the tip, although the polarisation was not retained on removal of the field. Similar behaviour has been observed previously in acceptor-doped normal ferroelectrics, although in that case it is generally attributed to domain wall pinning effects rather than the presence of PNRs.[30] On the other hand, for the quenched case, a nonlinear and strongly hysteretic *P–E* response was developed even at a field of 3 kV mm^{-1}, and a near-saturated loop was obtained at 6 kV mm^{-1}.

Temperature-dependent ferroelectric *P–E* hysteresis loops for both slow-cooled and quenched ceramics were measured at 6 kV mm^{-1} up to 150 °C, as illustrated in Fig. S2 (ESI†). Ferroelectric domain switching or domain wall movement in conventional ferroelectric-type ceramics can be enhanced by increasing temperature, resulting in reduced coercive field and higher switched polarisation values, as seen for the quenched case. Nonetheless, for the slow-cooled case, a gradual increase in polarisation and relatively larger increase at E_{Max} = 6 kV mm^{-1}, is observed. However, a constricted appearance of the *P–E* hysteresis loop was maintained. At a temperature of 150 °C, rounded hysteresis loops were observed for both the slow-cooled and quenched states, indicating increased leakage current due to thermally-activated conductivity.

It is known that the nucleation and growth of ferroelectric domains, together with their subsequent mobility, greatly impacts upon the macroscopic polarisation switching behaviour. It is speculated that grain boundaries act as pinning centres for the ferroelectric domains, thereby generally restricting the domain wall motion, which in turn reduces the magnitude of bulk polarization changes during external stimuli.[31] Based on this view, the absence of domain features in the shell regions of the slow-cooled ceramic could be used as a strong argument that the featureless shell can be treated as an intra-grain boundary that acts to restrain domain switching in the ferroelectric core, for electric field levels exceeding its coercive field. On the other hand, the observation of micro-sized ferroelectric domains in the shell region of the quenched ceramic indicates that the restrictive intragranular elastic constraint was diminished and an environment for effective domain wall mobility was created. Therefore, it can be concluded that the observed heterogeneous microstructure gives rise to heterogeneous polarisation switching mechanisms. In such a case, there is no need to invoke any defect-related pinning mechanisms to explain the constrained polarisation switching behaviour of the slow-cooled ceramic.

2.4 *In situ* investigation of microscopic actuation mechanisms

A polycrystalline ferroelectric ceramic subjected to an applied electric field will give rise to a unique diffraction pattern on the detector for each grain orientation, ψ, relative to the applied field direction, as illustrated schematically in Fig. 4(a). For example, the relative intensities of the *hhh*-type diffraction peaks in rhombohedral symmetry change due to the electric field-induced changes in crystallographic texture (*i.e.* preferred orientation of the non-180° ferroelectric domain structure), whereas peak shifts occur in *h*00-type peaks due to variations in the lattice spacing.[20,32] To monitor and quantify the contribution of such changes relative to the total electrostrain, it is necessary to determine the extrinsic and intrinsic contributions associated with domain switching and lattice strain, respectively.[20,32–34] Thus, certain crystallographic orientations such as {111}, {200} and {220} will be examined in order to make an initial assessment of the microscopic actuation mechanisms.

Diffraction patterns corresponding to ψ = 0° (*i.e.* representing grain families oriented with their scattering vectors parallel to the electric field) for the slow-cooled and quenched ceramics are shown in Fig. 4(b) and (c), respectively. These patterns correspond to the points where the electric field varies from 0 to ±6 kV mm^{-1} ($\pm E_{MAX}$), yielding 2 bipolar cycles in the triangular waveform, as illustrated in Fig. 4(d). It is evident that on increasing the electric field, the structural variations in the slow-cooled state were minimal and only a slight peak broadening was observed at $\pm E_{MAX}$. In contrast, the influence of the applied electric field on the peak profiles of {111}, {200} and {220} for the quenched ceramic was substantial, particularly at $\pm E_{MAX}$. After the removal of the field, peak splitting for {111} and {220} was more pronounced and a noticeable peak broadening was also observed for {200}. Qualitatively, these observations indicate that the electromechanical response in the slow-cooled state is minimal and cannot be assessed readily due to the presence of asymmetric peak broadening and lack of noticeable features. However, the pronounced variations in the {111}, {200} and {220} peak profiles for the quenched state show clear evidence of the ferroelectric domain switching phenomena and electric field-induced strain.

To quantify the microscopic strain for the slow-cooled and quenched ceramics, the {111} peak profile, which is the characteristic polar direction for rhombohedral symmetry, was de-convoluted into two peaks using a pseudo-Voigt function within Matlab. The effective average lattice strain associated with this grain orientation, x_{ψ}^{111}, was estimated on the basis of a simple weighted average of the diffraction peak positions. This operation was performed on particular grain orientations, with ψ = 0°, 30°, 60° and 90° (Fig. 5(a)). It was found that the variations in the strain, x_{111} as a function of grain orientation are consistent with the response of a typical rhombohedral ferroelectric.[20]

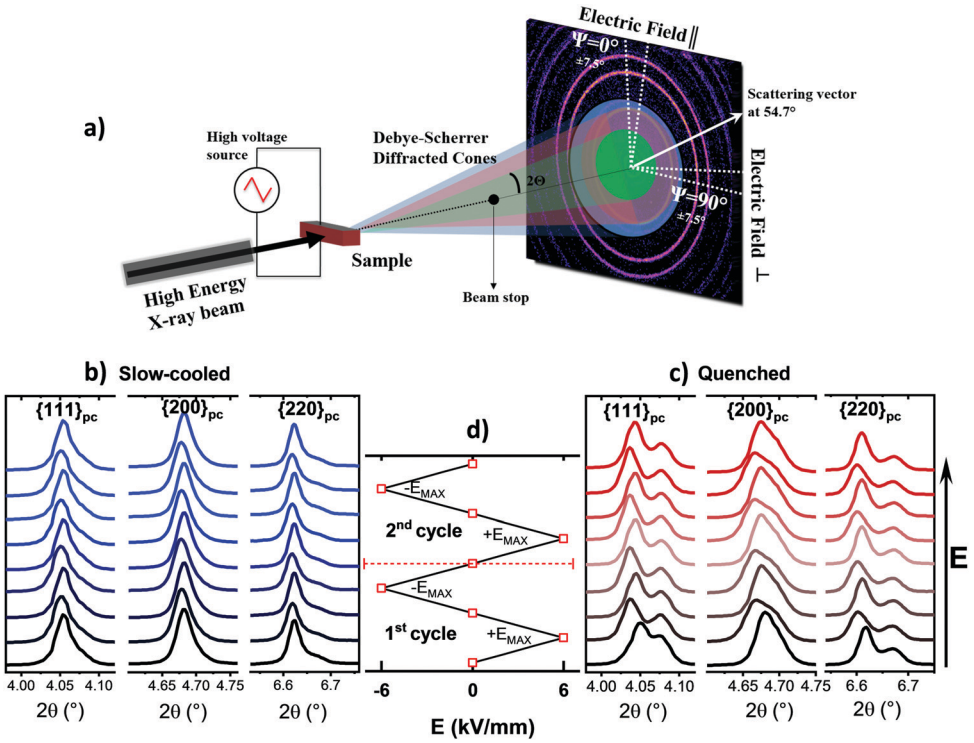

Fig. 4 (a) Experimental setup for *in situ* high-energy X-ray diffraction during application of electric field. Variations in diffraction profiles for {111}, {200} and {220} along the field direction (ψ = 0°): (b) slow-cooled and (c) quenched BF–BT–1Ti ceramics. 2 bipolar cycles of the applied electric field corresponding to each diffraction profile are also included in (d).

The largest positive strain was observed at ψ = 0°, for the quenched state, indicating development of tensile strain along the field direction; this was reduced in magnitude at 30° and diminished almost to zero at 60°, which is expected to be near the texture-free orientation of 54.7°. Subsequently, negative strains were observed at 90° due to development of compressive strain along the transverse direction. It is also evident that the application of the 2nd bipolar cycle to the quenched ceramic enhanced the symmetric shape of the loop. This observation indicates that re-orientation of domains under an electric field was stabilised

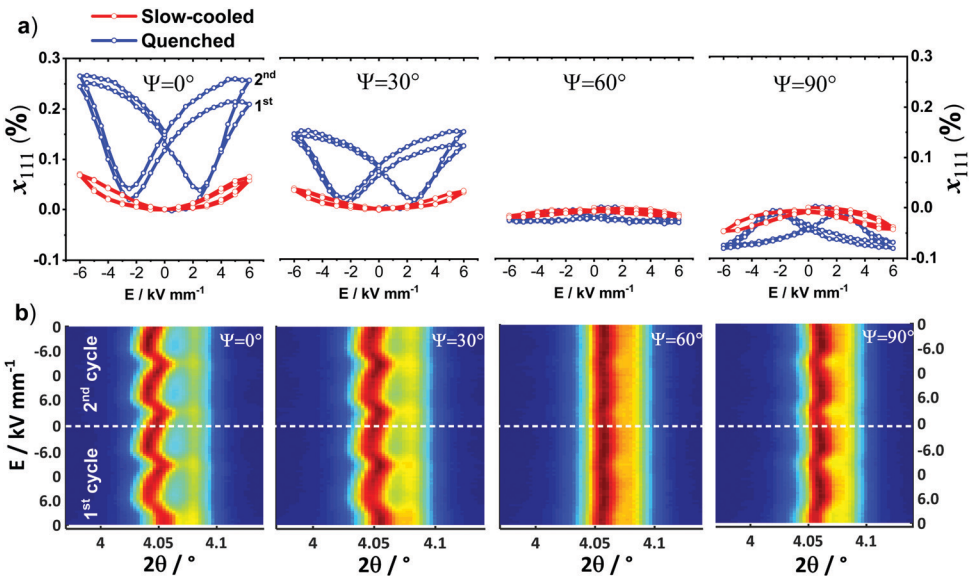

Fig. 5 (a) Calculated microscopic lattice strain contribution of {111}, x_{111}, in slow-cooled and quenched BF–BT–1Ti ceramics, in relation to the grain orientations, ψ of 0°, 30°, 60° and 90°. (b) Surface contour plots of {111} peak profiles for quenched ceramic as a function of applied electric field for the same grain orientations.

with subsequent cycling, which in turn led to a symmetric loop as a result of improved poling. On the other hand, by inspection of the surface contour plots for {111} given in Fig. 5(b), it appears that the characteristic preferred orientation in the (111) and ($\bar{1}$11) doublet, which is normally expected for domain switching in a typical rhombohedral ferroelectric, is absent.[20,32] Instead, there was a combination of large peak shift starting from $2\theta \approx 4.06^\circ$ and slight intensity fluctuations in the peak at $2\theta \approx 4.09^\circ$.

To seek a further indication of domain switching, the variations in the peak profile of the {222} reflection as a function of grain orientation were also examined, as shown in Fig. 6, for the quenched state. Similar to the behaviour of the {111} diffraction peak under the electric field, variations in the {222} peak profiles are predominantly composed of peak shifts and intensity fluctuations, which differ with grain orientation angle, ψ. However, from the diffraction profile of {222} in the remanent state (after the 1st cycle) plotted as a function of grain orientation (Fig. 6(b)), it can be seen that systematic intensity variations and hence preferred domain orientation can be identified with the assistance of the previous structural refinement presented in Fig. 2(a).

If we take the scattering angles corresponding to $R3c^{\mathrm{Core}}$ and $R3c^{\mathrm{Shell}}$ of {222} from the full-pattern refinement and position them on the plot, denoted as C and S, respectively (Fig. 6(b)), there is a close match with the observed large peak shift, indicating that it could be indeed a consequence of domain switching within the shell component. Since the rhombohedral distortion in the shell is not as large as that in the core, the individual peaks are not resolved and we observe significant peak shifts instead of the typical texturing in rhombohedral $R3c$ symmetry.[20,32] This introduces a complication in that the intrinsic and extrinsic contributions of the shell phase cannot be readily distinguished and therefore, for the following strain analysis, it is treated as an effective average lattice strain, which is a sum of the intrinsic and extrinsic contributions. On this basis, the strain contributions from the core and shell regions are quantified in the following section.

2.4.1 Determination of strain contributions for core and shell phases. The overall variations in the {111}, {200} and {220} peak profiles under the electric field with 0.5 kV mm^{-1} steps for the quenched ceramic are shown in Fig. 7(a), (b) and (c), respectively. It can be seen that upon application of the electric field, both intensity changes and peak shifts are present in all the reflections. This clearly indicates interplay of actuation mechanisms between domain switching and lattice strain (*i.e.* unit cell contraction/expansion). It is also apparent that there is no indication of any phase transformation for both $\pm E_{\mathrm{MAX}}$ and the remanent state, and therefore there is no need to account for this in the quantification of strain. Thus, the origin of electromechanical strain in the quenched state is attributed to a combination of non-180° domain switching and associated lattice deformation, in both core and shell regions. This can be resolved *via* individual peak fitting analysis in TOPAS and Matlab. We tested these two peak-fitting methods using various peak shape functions and concluded that individual peak fitting *via* TOPAS with the basis of structural refinement yielded better outcomes since it can readily distinguish between the corresponding core (C) and shell (S) phase peaks, as can be seen in Fig. 7(d)–(f) for the associated crystallographic orientations, and thus detailed structural information can accordingly be obtained.

The detailed fitting procedure employed the following steps:

(i) The {111}, {200} and {220} crystallographic orientations were evaluated to provide a representative weighted average,

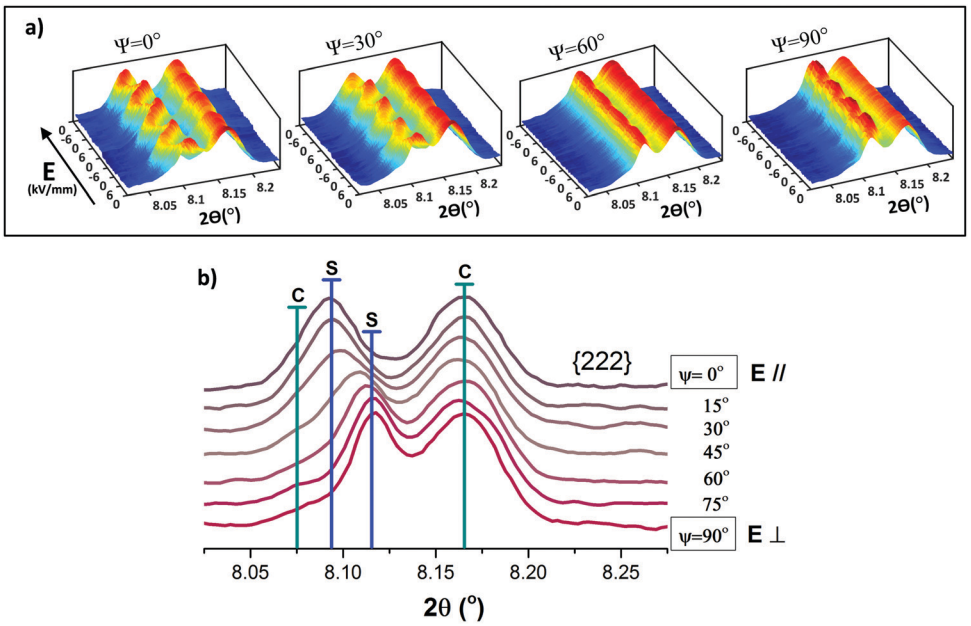

Fig. 6 (a) Contour plots of {222} diffraction pattern of quenched BF–BT–1Ti ceramic as a function of applied electric field for the grain orientations, ψ of 0°, 30°, 60° and 90°. (b) Identification of intensity variations in core (C) and shell (S) peaks as a function of grain orientation in the remanent state, after removal of the electric field.

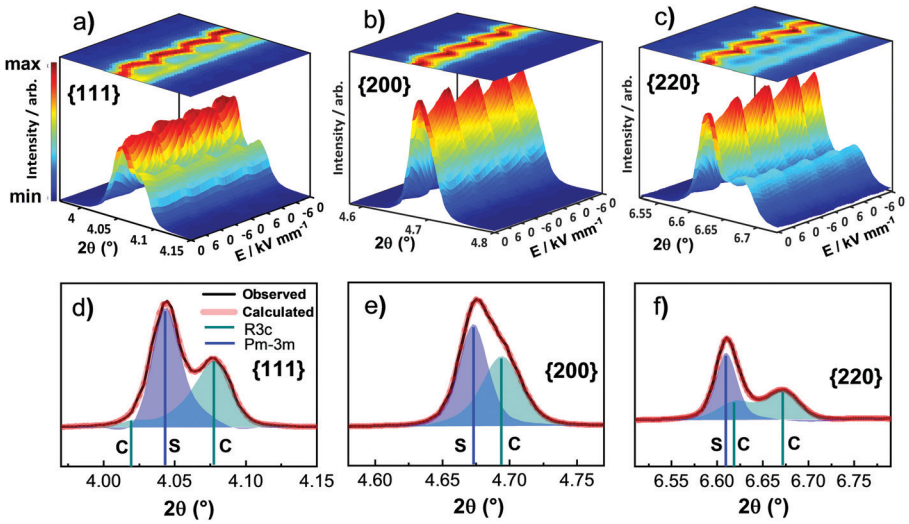

Fig. 7 Evolution of (a) {111}, (b) {200} and (c) {220} diffraction peak profiles under 2 bipolar cycles of electric field in the quenched ceramic. Individual peak fitting is illustrated underneath the corresponding contour plots, as shown in (d)–(f). The fitted data is taken from the remanent state of the 1st cycle. *R3c* and *Pm*$\bar{3}$*m* phase contributions are abbreviated as C and S, referring to core and shell phases, respectively.

enabling an estimation of the total macroscopic strain of the polycrystal.[35] Full pattern fitting of the diffraction patterns obtained under an applied electric field was not considered to be appropriate due to elastic interactions between differently-oriented grains together with anisotropy of elastic and piezoelectric properties, which are not currently accounted for within standard diffraction software.

(ii) An initial attempt was made to fit the individual diffraction peak profiles with $R3c^{\mathrm{Core}}$ and $R3c^{\mathrm{Shell}}$ phases, as suggested by the structural refinement in Fig. 2(a). However, it was challenging to extract the individual intensities of the (111) and ($\bar{1}$11) peaks for the fitted shell phase, due to a combination of peak broadening and the limited resolution of the detector. This problem is exacerbated since the rhombohedral lattice distortion in the shell (η_{rh} = 0.18%) was relatively small in comparison with that of the core (η_{rh} = 1.2%), as given in Table S1 (see the ESI†). Therefore, the crystal structure of the shell phase was approximated as pseudocubic *Pm*$\bar{3}$*m*.

(iii) Asymmetric and broad peaks were fitted by de-convoluting into three peaks for {111} and {220}, and two peaks for {200}. The modified Pseudo-Voigt function (PV-TCHZ) was used to extract the information from which the structural parameters of the associated core and the shell phases (*e.g.* magnitude of integrated intensity, inter-planar lattice spacing, structure factors) were determined.

Based on the fitting procedure described above, the crystal structure is now considered to comprise a combination of $R3c^{\mathrm{Core}}$ and $Pm\bar{3}m^{\mathrm{Shell}}$ phases. Each phase fraction, f_n can be then determined by

$$f_n = \frac{\left[\dfrac{I_n^{hkl}}{m_n^{hkl}\left|F_n^{hkl}\right|^2}\right]}{\sum_n \left[\dfrac{I_n^{hkl}}{m_n^{hkl}\left|F_n^{hkl}\right|^2}\right]} \quad (4)$$

where I_n^{hkl}, m_n^{hkl} and $|F_n^{hkl}|^2$ are the integrated intensity, multiplicity and squared structure factor of the associated nth reflections hkl of core (C) and shell (S) phases as highlighted in Fig. 6(b). The phase fractions corresponding to core and shell regions are related by $f_1 + f_2 + f_3 = 1$; where $n = 1$ was used to represent the shell phase, while $n = 2$ and $n = 3$ represent (111) and ($\bar{1}$11) domain orientations of the core respectively, and calculated accordingly using eqn (4).

The structure factors for each hkl were obtained from the full-pattern structure refinement of the unpoled (randomly-oriented) ceramic. During this peak fitting analysis, the phase fraction of $Pm\bar{3}m^{\mathrm{Shell}}$ was found to be around 60% and it was invariant under the electric field variation, for $\psi = 0^\circ$. Therefore, the electric field-induced phase transformation was disregarded in the following strain calculations.

Subsequently, the average effective d-spacing at zero electric field, $d_{\mathrm{total}}^{hkl^0}$, and under the electric field d_{total}^{hkl} can be expressed in relation to the corresponding phase fractions obtained from eqn (4), $f_n^{hkl^0}$ and f_n^{hkl}, as follows:

$$d_{\mathrm{total}}^{hkl} = \sum_n f_n^{hkl} d_n^{hkl} \quad (5)$$

$$d_{total}^{hkl^0} = \sum_n f_n^{hkl^0} d_n^{hkl^0} \quad (6)$$

The total microscopic strain for each grain orientation, ε_{hkl}, can then be calculated according to eqn (7).

$$x_{hkl} = \frac{d_{\mathrm{total}}^{hkl} - d_{\mathrm{total}}^{hkl^0}}{d_{\mathrm{total}}^{hkl^0}} \quad (7)$$

The calculated microscopic strain results for {111}, {200} and {220} grain orientations are shown in Fig. 8(a), (b) and (c), respectively. Microscopic strain variations for the core and shell regions show clear evidence of strain heterogeneity on the micro scale within the grains. The field-induced strain in the

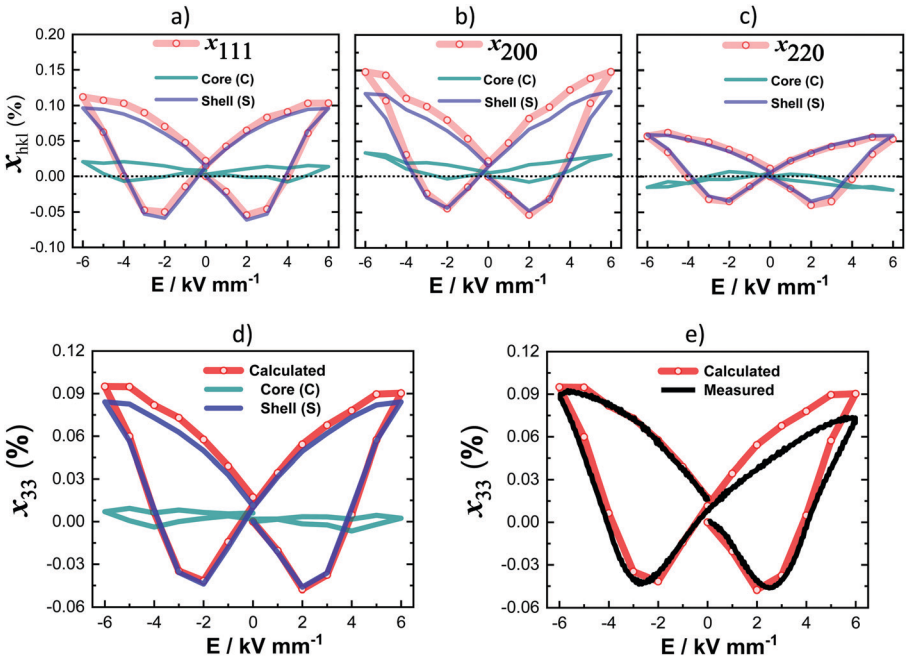

Fig. 8 Calculated microscopic strain obtained from individual crystallograpic planes of (a) {111}, (b) {200} and (c) {220} under the application of bipolar electric field, including core (C) and shell (S) contributions. (d) Calculated core and shell strain contributions to the total strain obtained from the *in situ* study and (e) comparison of measured (macroscopic) and calculated total strain–electric field responses.

rhombohedral core was generally much lower than that in the shell, for all grain orientations, indicating that the more-active shell regions were actually subject to elastic constraint by the less-active core regions. This strain heterogeneity must cause significant intra-granular stress. Differences in strain were also observed between the different grain orientations, due to piezoelectric and elastic anisotropy, which indicates the development of inter-granular stresses.

It should be noted that overlapping of the selected diffraction peaks corresponding to core and shell phases as observed in Fig. 7(d) and (f) may cause relatively large uncertainties and deviations in the individual contribution to the strain profiles. Thus, a further modification is required for reliable strain determination, as described in the following section.

The macroscopic strain was estimated based on the weighted average of the effective lattice strains associated with different crystallographic orientations, according to the equation shown below[32,36]

$$x_{33}(\psi) = \frac{\sum_{hkl} T_{hkl} m_{hkl} x_{hkl}(\psi)}{\sum_{hkl} T_{hkl} m_{hkl}} \quad (8)$$

where $x(\psi)$ is the component of the macroscopic strain tensor for a given orientation, $x_{hkl}(\psi)$ is the local lattice strain along the axis parallel to direction ψ for the $\{hkl\}$ orientation, T_{hkl} is the texture index, and m_{hkl} is the multiplicity of the reflection for $\{hkl\}$ planes. Treating the material as cubic and with random grain texture, T_{hkl} reduces to 1 for any hkl, and m_{hkl} is 8, 6, and 12 for {111}, {200}, and {220} orientations, respectively.

The total longitudinal strain, x_{33}, was calculated in terms of a volume weighted average of the different effective lattice strains, x_{hkl}, measured parallel to the applied electric field direction, $\psi = 0^\circ$. The calculated results are illustrated in Fig. 8(d), comparing each contribution of core and shell phases as well as the net macroscopic strain. It is evident that the macroscopic strain obtained from the shell is predominant, while the core contribution is almost negligible, indicating that the observed large electromechanical actuation is a result of mainly one component in the electric field range up to 6 kV mm^{-1}. These results are consistent with the presence of a $BiFeO_3$-rich core having a coercive field significantly higher than those accessed during the present study.

On the other hand, strain anisotropy and elastic coupling parameters must also be taken into account when analysing heterogeneous-type actuation mechanisms associated with a grain and its surroundings. The cyclic variations in lattice strain for {111}, {200} and {220} as a function of frame number along the electric field direction, $\psi = 0^\circ$, are shown in Fig. S4a (ESI†). It can be seen that the largest strain contribution was from {200} grain families, which tends to contradict the expected dominance of the polar ⟨111⟩ directions for materials exhibiting rhombohedral crystal structure. It should be noted that although the shell phase has been refined as rhombohedral structure with reduced rhombohedral lattice distortion and octahedral tilting, it was characterised as $Pm\bar{3}m$ during peak profile fitting due to the relatively low resolution. Although strain anisotropy in the grain families of {111}, {200} and {220} is apparent, normalisation of x_{111}, x_{200} and x_{220} depicted in Fig. S4b (ESI†) shows that the cyclic strains induced by the electric field in these grain families are strongly correlated due to elastic coupling between grains having different crystallographic orientations. It has been reported recently that in structurally heterogeneous

regions such as near phase boundaries in $BiFeO_3$-based ceramics, field-induced phase transformation dynamics and rates are particularly important to obtain high electromechanical response.[37,38] However, there is no evidence of any such electric field-induced phase transformations in the present results.

The accuracy of the calculated total strain is evaluated in Fig. 8(e) by comparison with the macroscopic strain–electric field data, measured on a different test specimen using an AixACCT TF 2000 system. It is apparent that the calculated *S*–*E* loop is highly symmetric with a good match on the negative side of electric field, but showing a discrepancy with the asymmetric macroscopic strain measurement for positive fields. This discrepancy is attributed primarily to differences in the experimental procedures employed for the 2 methods, with a much shorter measurement time being employed for the macroscopic measurement in comparison with the *in situ* diffraction study (10 s compared with 500 s for a single cycle).

The results presented here show that the shell phase comprises approximately 60% of the total phase content (Table S1 of the ESI†) in the quenched state and provides almost 93% strain contribution to the maximum total strain (x_{33}^{shell} = 0.13%; x_{33}^{total} = 0.14%). From the dielectric permittivity data presented in Fig. 3(b), it is concluded that the broad lower-temperature peak in the ε_r–*T* relationship is associated with the $BaTiO_3$-rich shell phase. Since T_m^1 is significantly lower than T_m^2, it is highly probable that the room temperature permittivity of the shell regions is higher than that of the core phase and consequently the electrostrictive contribution to strain is larger. Furthermore, the lower Curie temperature for the shell phase should yield a lower ferroelectric coercive field and hence improved domain switching behaviour. Both of these factors contribute to the observed dominant strain response from the shell regions.

Based on this observation, it is evident that higher electromechanical performance could be obtained in a material comprising solely or major shell phase having the appropriate composition. It should also be noted that the shell phase is prone to be $BiFeO_3$-deficient, which means that the reduction of $BiFeO_3$ content is necessary. However, this may significantly reduce the Curie temperature of the solid solution system. Such a trade-off in the functional properties should be carefully adjusted according to either the BF/BT ratio, covering a wide compositional range of BF–BT solid solutions, or the volume fractions of core and shell phases in a selected composition with pre- (doping trials) or post-processing (thermal treatments) methods.

Another aspect to consider is that the core–shell microstructure was not synthesized intentionally in this study, whereas it is a common feature in 0–3 type composites[39–41] or for $BaTiO_3$-based ceramic capacitors,[42,43] for example. In the present case, it is a result of kinetic and thermodynamic factors, associated with differences in the reactivity of the precursor oxides/carbonates and immiscibility between $BiFeO_3$- and $BaTiO_3$-rich phases respectively. In common with our previous study[6] we suppose that the incorporation of a minor amount of donor dopant (Ti^{4+} for Fe^{3+}) hinders grain growth and homogenisation of the solid solution during high temperature sintering. It is important to emphasise that although the ferroelectric $BiFeO_3$ core is relatively inactive upon the application of an electric field, based on its negligible contribution to the total strain, it plays a critical role in forming the nucleus within the self-grown core–shell microstructure, which could indeed be of great interest and advantageous in various applications including high temperature ultrasonic transducers, dielectric energy storage and magnetoelectric devices.

3. Conclusions

Thorough and comparative investigations were carried out to evaluate the influence of cooling method on the structure and functional properties of heterogeneous 1 mol% Ti-substituted BF–BT piezoceramics with an emphasis on the electromechanical actuation mechanisms. Structural and microstructural investigations show clear evidence of chemical segregation. The segregated regions were then assigned as core and shell phases. Their effects on the functional properties were analysed based on their ferroelectric nature and the influence of cooling conditions. The crystal structure of the shell region is shown to comprise pseudocubic ($Pm\bar{3}m$) in the slow-cooled state and untilted rhombohedral phase ($R3m$) in the quenched state, whilst the core region is defined as a highly distorted rhombohedral phase with $R3c$ space group in both cases. The mechanisms that contribute to the electric field-induced strain are evaluated by considering both the intrinsic and extrinsic contributions from each phase through the use of *in situ* synchrotron X-ray diffraction, illustrating a good agreement with macroscopic strain measurements. The total peak-to-peak strain is found to be $x_{33} \approx 0.14\%$; the transformed shell is actively involved in the electric field-induced actuation mechanism ($x_{33} \approx 0.13\%$), while the rhombohedral core is almost inactive upon poling, which yields negligible strain response ($x_{33} \approx 0.01\%$). The diffraction results demonstrate the presence of a heterogeneous, constrained actuation mechanism that can be readily observed after thermal quenching in core–shell structured $BiFeO_3$–$BaTiO_3$ ceramics and may provide a novel route for the development of next generation piezoceramics.

4. Experimental method

Experimental details are provided in the ESI.†

Conflicts of interest

There are no conflicts of interest to declare.

Acknowledgements

We thank Diamond Light Source for access to beamline I15 (proposal number EE16390) that contributed to the results presented here. I. Calisir thanks the National Education of Turkish Republic for financial support throughout his PhD.

Notes and references

1 K. Uchino, Piezoelectric Energy Harvesting Systems—Essentials to Successful Developments, *Energy Technol.*, 2018, **6**, 829–848.
2 K. Uchino, Glory of piezoelectric perovskites, *Sci. Technol. Adv. Mater.*, 2015, **16**, 046001.
3 J. Rödel, *et al.*, Perspective on the Development of Lead-free Piezoceramics, *J. Am. Ceram. Soc.*, 2009, **92**, 1153–1177.
4 G. Catalan and J. F. Scott, Physics and applications of bismuth ferrite, *Adv. Mater.*, 2009, **21**, 2463–2485.
5 S. M. Selbach, T. Tybell, M. A. Einarsrud and T. Grande, The ferroic phase transitions of $BiFeO_3$, *Adv. Mater.*, 2008, **20**, 3692–3696.
6 I. Calisir, A. A. Amirov, A. K. Kleppe and D. A. Hall, Optimisation of functional properties in lead-free $BiFeO_3$–$BaTiO_3$ ceramics through La^{3+} substitution strategy, *J. Mater. Chem. A*, 2018, **6**, 5378–5397.
7 I. Calisir and D. A. Hall, Chemical heterogeneity and approaches to its control in $BiFeO_3$–$BaTiO_3$ lead-free ferroelectrics, *J. Mater. Chem. C*, 2018, **6**, 134–146.
8 S. O. Leontsev and R. E. Eitel, Dielectric and Piezoelectric Properties in Mn-Modified (1-x)$BiFeO_3$–x$BaTiO_3$ Ceramics, *J. Am. Ceram. Soc.*, 2009, **92**, 2957–2961.
9 T. Rojac, *et al.*, $BiFeO_3$ Ceramics: Processing, Electrical, and Electromechanical Properties, *J. Am. Ceram. Soc.*, 2014, **97**, 1993–2011.
10 M. H. Lee, *et al.*, High-performance lead-free piezoceramics with high Curie temperatures, *Adv. Mater.*, 2015, **27**, 6976–6982.
11 J. Wei, D. Fu, J. Cheng and J. Chen, Temperature dependence of the dielectric and piezoelectric properties of $x$$BiFeO_3$–$(1-x)$$BaTiO_3$ ceramics near the morphotropic phase boundary, *J. Mater. Sci.*, 2017, **52**, 10726–10737.
12 S. Shen, *et al.*, The effect of cooling rate on structural and electrical properties of multiferroic BLF-PT ceramics, *J. Am. Ceram. Soc.*, 2018, 1–6.
13 D. S. Kim, C. Il Cheon, S. S. Lee and J. S. Kim, Effect of cooling rate on phase transitions and ferroelectric properties in $0.75BiFeO_3$–$0.25BaTiO_3$ ceramics, *Appl. Phys. Lett.*, 2016, **109**, 202902.
14 T. Zheng, C. Zhao, J. Wu, K. Wang and J. F. Li, Large strain of lead-free bismuth ferrite ternary ceramics at elevated temperature, *Scr. Mater.*, 2018, **155**, 11–15.
15 T. Rojac, M. Kosec, B. Budic, N. Setter and D. Damjanovic, Strong ferroelectric domain-wall pinning in $BiFeO_3$ ceramics, *J. Appl. Phys.*, 2010, **108**, 074107.
16 S. Kim, *et al.*, Revealing the role of heat treatment in enhancement of electrical properties of lead-free piezoelectric ceramics, *J. Appl. Phys.*, 2017, **122**, 014103.
17 U. Robels and G. Arlt, Domain wall clamping in ferroelectrics by orientation of defects, *J. Appl. Phys.*, 1993, **73**, 3454–3460.
18 D. Damjanovic, Hysteresis in piezoelectric and ferroelectric materials, *The Science of Hysteresis*, 2006, vol. 3.
19 A. M. Glazer, The classification of tilted octahedra in perovskites, *Acta Crystallogr., Sect. B: Struct. Crystallogr. Cryst. Chem.*, 1972, **28**, 3384–3392.
20 D. A. Hall, *et al.*, Domain switching in rhombohedral PZT ceramics under electrical and mechanical loading, *Mater. Sci. Technol.*, 2008, **24**, 927–933.
21 Y. Yoneda, K. Yoshii, S. Kohara, S. Kitagawa and S. Mori, Local structure of $BiFeO_3$–$BaTiO_3$ mixture, *Jpn. J. Appl. Phys.*, 2008, **47**, 7590–7594.
22 M. M. Kumar, A. Srinivas and S. V. Suryanarayana, Structure property relations in $BiFeO_3$/$BaTiO_3$ solid solutions, *J. Appl. Phys.*, 2000, **87**, 855–862.
23 A. Singh, C. Moriyoshi, Y. Kuroiwa and D. Pandey, Evidence for local monoclinic structure, polarization rotation, and morphotropic phase transitions in $(1-x)$$BiFeO_3$–$x$$BaTiO_3$ solid solutions: a high-energy synchrotron X-ray powder diffraction study, *Phys. Rev. B: Condens. Matter Mater. Phys.*, 2013, **88**, 024113.
24 R. Kiyanagi, *et al.*, Structural and magnetic phase determination of $(1-x)$$BiFeO_3$–$x$$BaTiO_3$ solid solution, *J. Phys. Soc. Jpn.*, 2012, **81**, 024603.
25 M. Hinterstein, *et al.*, Cyclic electric field response of morphotropic $Bi_{1/2}Na_{1/2}TiO_3$–$BaTiO_3$ piezoceramics, *Appl. Phys. Lett.*, 2015, **106**, 222904.
26 D. H. Megaw and C. N. W. Darlington, Geometrical and Structural Relations in the Rhombohedral Perovskites, *Acta Crystallogr., Sect. A: Cryst. Phys., Diffr., Theor. Gen. Crystallogr.*, 1975, **31**, 161–173.
27 F. Kubel and H. Schmid, Structure of a ferroelectric and ferroelastic monodomain crystal of the perovskite $BiFeO_3$, *Acta Crystallogr., Sect. B: Struct. Sci.*, 1990, **46**, 698–702.
28 M. Dolgos, *et al.*, Chemical control of octahedral tilting and off-axis A cation displacement allows ferroelectric switching in a bismuth-based perovskite, *Chem. Sci.*, 2012, **3**, 1426.
29 F. Li, S. Zhang, D. Damjanovic, L. Q. Chen and T. R. Shrout, Local Structural Heterogeneity and Electromechanical Responses of Ferroelectrics: Learning from Relaxor Ferroelectrics, *Adv. Funct. Mater.*, 2018, **1801504**, 1–21.
30 L. Jin, F. Li and S. Zhang, Decoding the Fingerprint of Ferroelectric Loops: Comprehension of the Material Properties and Structures, *J. Am. Ceram. Soc.*, 2014, **97**, 1–27.
31 S. Mantri, J. Oddershede, D. Damjanovic and J. E. Daniels, Ferroelectric domain continuity over grain boundaries, *Acta Mater.*, 2017, **128**, 400–405.
32 A. Pramanick, D. Damjanovic, J. E. Daniels, J. C. Nino and J. L. Jones, Origins of Electro-Mechanical Coupling in Polycrystalline Ferroelectrics During Subcoercive Electrical Loading, *J. Am. Ceram. Soc.*, 2011, **94**, 293–309.
33 D. A. Hall, A. Steuwer, B. Cherdhirunkorn, T. Mori and P. J. Withers, A high energy synchrotron X-ray study of crystallographic texture and lattice strain in soft lead zirconate titanate ceramics, *J. Appl. Phys.*, 2004, **96**, 4245–4252.
34 D. Ghosh, *et al.*, Domain wall displacement is the origin of superior permittivity and piezoelectricity in $BaTiO_3$ at intermediate grain sizes, *Adv. Funct. Mater.*, 2014, **24**, 885–896.
35 L. Daniel, *et al.*, Revisiting the blocking force test on ferroelectric ceramics using high energy X-ray diffraction, *J. Appl. Phys.*, 2015, **117**, 174104.
36 J. E. Daniels, T. R. Finlayson, A. J. Studer, M. Hoffman and J. L. Jones, Time-resolved diffraction measurements of

electric-field-induced strain in tetragonal lead zirconate titanate, *J. Appl. Phys.*, 2007, **101**, 094104.

37 J. Walker, *et al.*, Temperature dependent piezoelectric response and strain–electric-field hysteresis of rare-earth modified bismuth ferrite ceramics, *J. Mater. Chem. C*, 2016, **4**, 7859–7868.

38 J. Ormstrup, *et al.*, Dynamics and grain orientation dependence of the electric field induced phase transformation in Sm modified $BiFeO_3$ ceramics, *J. Mater. Chem. C*, 2018, **6**, 7635–7641.

39 J. Ma, J. Hu, Z. Li and C. W. Nan, Recent progress in multiferroic magnetoelectric composites: from bulk to thin films, *Adv. Mater.*, 2011, **23**, 1062–1087.

40 C. A. F. Vaz, J. Hoffman, C. H. Ahn and R. Ramesh, Magnetoelectric coupling effects in multiferroic complex oxide composite structures, *Adv. Mater.*, 2010, **22**, 2900–2918.

41 X. Qi, *et al.*, A ferroelectric ferromagnetic composite material with significant permeability and permittivity, *Adv. Funct. Mater.*, 2004, **14**, 920–926.

42 M.-J. Pan and C. A. Randall, A Brief Introduction to Ceramic, *IEEE Electr. Insul. Mag.*, 2010, **26**, 44–50.

43 H. Kishi, Y. Mizuno and H. Chazono, Base-metal electrode-multilayer ceramic capacitors: past, present and future perspectives, *Jpn. J. Appl. Phys., Part 1*, 2003, **42**, 1–5.